Semiconductor heterostructures and optimization of light-trapping structures for efficient thin-film solar cells

2012 J. Opt. 14 024007

(http://iopscience.iop.org/2040-8986/14/2/024007)

J. Opt. **14** (2012) 024007 (11pp) doi:10.1088/2040-8978/14/2/024007

Semiconductor heterostructures and optimization of light-trapping structures for efficient thin-film solar cells

Claiborne O McPheeters[1], Dongzhi Hu[2], Daniel M Schaadt[2] and Edward T Yu[1]

[1] Microelectronics Research Center, Department of Electrical and Computer Engineering, The University of Texas at Austin, Austin, TX 78758, USA
[2] DFG—Center for Functional Nanostructures, Karlsruhe Institute of Technology, 76131 Karlsruhe, Germany

E-mail: ety@ece.utexas.edu

Received 7 July 2011, accepted for publication 20 September 2011
Published 12 January 2012
Online at stacks.iop.org/JOpt/14/024007

Abstract
Sub-wavelength photonic structures and nanoscale materials have the potential to greatly improve the efficiencies of solar cells by enabling maximum absorption of sunlight. Semiconductor heterostructures provide versatile opportunities for improving absorption of infrared radiation in photovoltaic devices, which accounts for half of the power in the solar spectrum. These ideas can be combined in quantum-well solar cells and related structures in which sub-wavelength metal and dielectric scattering elements are integrated for light trapping. Measurements and simulations of GaAs solar cells with less than one micron of active material demonstrate the benefits of incorporating In(Ga)As quantum-wells and quantum-dots to improve their performance. Simulations that incorporate a realistic model of absorption in quantum-wells show that the use of broadband photonic structures with such devices can substantially improve the benefit of incorporating heterostructures, enabling meaningful improvements in their performance.

Keywords: quantum-well, quantum-dot, scattering, diffraction, thin-film, GaAs, InAs, photovoltaic, solar cell

(Some figures in this article are in colour only in the electronic version)

1. Introduction

Renewable energy has become a subject of great interest as a result of concerns about the cost, availability, environmental effects, and political and social implications associated with traditional forms of energy generation. Continuing advances in photovoltaic technology and its relevance to powering equipment in space has led to dramatic recent progress in the development of solar cells for both terrestrial and space applications. However, one of the most persistent issues in solar cell design continues to be how to most effectively address the fundamental tradeoff between light absorption and carrier collection. The use of sub-wavelength structures and nanostructured materials to improve absorption in photovoltaic devices, often by increasing the path length of light as a result of scattering or diffraction, is a powerful approach for addressing this tradeoff.

In this regard, nanostructured materials are enabling new possibilities for the design and integration of active and passive media in solar cells. Myriad photonic structures containing sub-wavelength features have been proposed for improving photovoltaic device performance, including diffraction gratings [1–3], nanoparticles [4–8], and photonic crystals [9–12]. Meanwhile, the unique properties of semiconductor nanostructures have inspired a host of new solar cell structures, including designs based on quantum-wells [13–15], quantum-dots [16–18], and nanowires [19–22]. Theoretical analyses of certain device concepts based on nanostructures [23–26] have shown that they can exceed the Shockley–Queisser efficiency limit for solar energy conversion

by single-bandgap devices by 31% [27]. Thus, extensive efforts are now being devoted to demonstrating and developing devices with nanostructured photonic and active media.

Simultaneously, there is great interest in thin-film devices to drive down the cost of solar photovoltaic energy and for new applications, e.g. energy harvesting for portable electronics. The light-weight, potentially flexible form factors of thin-film solar cells [28–31] make them attractive for aerospace and consumer markets. Their efficiencies, however, are typically lower than those of bulk devices because of reduced absorption in the thin material, particularly at infrared wavelengths, which account for half of the power in the solar spectrum. Thus, efforts are being made to establish optimal device structures for thin-film solar cells with the hope that they will be cost-effective for diverse applications.

In this paper, we address a number of these topics through discussion of design considerations for engineering photon propagation in solar cells, particularly with respect to thin-film devices, and present results of their application to the case of thin-film devices containing quantum-wells and quantum-dots. Material and design considerations related to quantum-well and -dot based solar cells are discussed and a semi-empirical approach to calculating the modified optical properties in quantum-wells and -dots illustrates significant implications for design and optimization of devices that contain them. Results of the fabrication of thin-film devices, together with simulation results, indicate that quantum-wells and -dots combined with effective light-scattering and -trapping structures can be used to achieve meaningful improvements in thin-film solar cell performance.

2. Approaches to scattering and trapping of light

Because the probability that light transmitted into a solar cell will be absorbed increases with the path length of photons in the device, materials and structures that increase photon path lengths can be essential for improving the performance of photovoltaic devices. Traditionally, this has been achieved by the use of micron-sized features, often with random geometries, to scatter incident radiation into the device. More recently, technological advancements have enabled the fabrication of structures that have the potential to significantly improve light transmission into and within photovoltaic devices. Yablonovitch identified the ability of textured surfaces to increase absorption in weakly absorbing materials by a factor of up to $4n^2$ [32], where n is the refractive index. Subsequent analyses have shown that greater enhancement factors are possible in thin-films [33–35], though realizing them over a wide range of wavelengths, polarization, and incident angles has only been theoretically demonstrated and requires complicated nanoscale structures [36]. Nevertheless, as fabrication and synthesis techniques for such structures have advanced, so has interest in them for improving the efficiency of solar cells.

Nanoscale particles, which can be relatively easily fabricated and integrated onto solar cell surfaces, have been of considerable interest for scattering and trapping of light in photovoltaics. Studies of the effects of both metal and dielectric nanoparticles deposited on the surface of photovoltaic devices have demonstrated broadband enhancement of photogenerated current and increased power conversion efficiencies relative to devices without nanoparticles [6, 7, 37–39], and provided substantial initial understanding of these and related effects. Such particles can be deposited or fabricated on the surface of a device in random [4–7] or geometric patterns [40–42]. In most cases, their essential function is to scatter light such that photon path lengths increase compared to those of photons that are directly transmitted at normal incidence into the device, thereby increasing the fraction of absorbed radiation. The scattering cross-sections of nanoparticles can exceed their geometric cross-sections, and their angular scattering distributions can be tuned with their size, shape, and composition [43], making nanoparticles a versatile option for studying light management in photovoltaics. Nanowires can also exhibit scattering properties and greater-than-unity interaction cross-sections [44–46], which, combined with their potential to achieve superior carrier transport and collection compared to bulk devices, has inspired studies of nanowires for photovoltaic applications.

Numerous studies of nanoparticles for enhancement of photovoltaics have focused on metal particles that exhibit surface plasmon polariton (SPP) resonances. This is partly a result of indications that the strong evanescent field associated with SPPs near the active region of a device can increase photocurrent generation. The possibility of destructive interference between the scattered and directly transmitted waves to inhibit photocurrent generation, which results from a phase difference between the waves near the SPP resonance [47], can be minimized or eliminated by careful choice of the material and size of nanoparticles with respect to the local dielectric environment.

Plasmonic effects and their application to improving photovoltaic device performance continue to be subjects of concerted research efforts. In addition to potential photocurrent enhancements associated with their strong evanescent fields, SPPs can mediate coupling to waveguide modes of photovoltaic devices and support confined plasmonic modes. The absorption and scattering cross-sections of sub-wavelength metallic structures are typically large near SPP resonant wavelengths, and efficient coupling of scattered light to waveguide modes of a thin-film device can occur if the momentum of scattered light matches that of a confined mode. The evanescent field of SPPs may also increase the intensity of radiation that couples to waveguide modes relative to light scattered at non-resonant wavelengths. Plasmonic effects do, however, increase absorption by the metal and will generally result in greater ohmic loss of energy than would occur in their absence. For this reason, and because of the potential for scattered fields associated with them to destructively interfere with others, the use of plasmonic structures for solar cell enhancement must be carefully engineered based on material and device properties and the solar spectrum.

The rational design of sub-wavelength structures for light trapping in solar cells is also an extremely active area of research. These structures typically exhibit variations on length scales similar to the wavelengths targeted for

diffraction or scattering. Despite their small feature sizes, advanced lithographic techniques can be used to pattern such structures over large areas [48–50]. Their design and optimization are typically performed numerically and both periodic [3, 11, 51, 52] and pseudo-random structures [53, 54] can be addressed with such approaches. As periodic structures, such as diffraction gratings, typically produce narrow response bands, optimal periodic structures for scattering of solar radiation are likely to have intricate geometries to handle a relatively broad band of wavelengths, different polarizations, and angles of incidence. Rigorous simulation of truly random structures is especially challenging, in particular because of the significant computational requirements to perform electromagnetic field calculations over large areas. Calculations that use periodic boundary conditions with random geometries to simulate pseudo-random structures are generally much more feasible. As optimal structures are likely to vary depending on the absorbing material of a solar cell and its operating conditions, the rational design of light-scattering structures is likely to be a topic of interest for the foreseeable future.

3. Quantum-wells and quantum-dots for solar cells

A complementary route to improving the efficiency of solar cells is by incorporating semiconductor heterostructures, which are typically quantum-wells or -dots in this context, to increase the range of their spectral response. Quantum-wells and -dots generally consist of well (or dot) material with a smaller bandgap than the barrier material that surrounds them, and well/dot thicknesses that are typically in the range of a few to tens of nanometers, where quantum confinement effects are important. Inserting such structures in the intrinsic layer of a pin diode improves its spectral matching to solar radiation by enabling absorption of light below the bandgap of the barrier material. The use of quantum-dots to realize an intermediate band device [18, 55] and to achieve multiple carrier generation from absorption of single photons [56, 57] is also being widely explored.

Fabrication of solar cells incorporating quantum-wells and -dots requires precise epitaxial growth of semiconductors, including control of the thickness of epilayers, design and realization of optimal doping profiles, and growth of atomically sharp interfaces. Epitaxial growth by molecular beam epitaxy (MBE) enables precise control of such properties, and is one of the standard approaches for fabricating complex semiconductor structures. All solar cell device structures in this work have been prepared by MBE at 500 °C using silicon and beryllium as n-type and p-type dopants, respectively, for their superior performance in MBE-grown GaAs [58, 59]. That growth temperature was chosen in consideration of the In(Ga)As materials; at 500 °C, the areal density, size, and composition of InAs quantum-dots, which are formed via self-assembly in the Stranski–Krastanov growth mode on GaAs (001) surfaces, can be adjusted by varying the duration of strain-induced coalescence of dots [60]. This offers an opportunity to deliberately study the influence of quantum-dots on the efficiency of the devices. It is important to note that the growth of In(Ga)As at temperatures above 490 °C can degrade material quality due to segregation of indium [61]. This effect can, however, be mitigated by inserting a thin AlAs layer above the quantum-dot or -well layers [62].

Figure 1 illustrates the typical thin-film device structure used in these studies, grown in all cases on 2 in n-type (001) GaAs wafers. Following a 200 nm buffer layer of undoped GaAs, a nominally undoped 800 nm layer of $Al_{0.85}Ga_{0.15}As$ is grown to serve as an etch stop for the substrate removal process, which is discussed in section 5. Growth of the epitaxial device layers follows. They consist of: 100 nm p^+-GaAs; a 40 nm p^+-$Al_{0.85}Ga_{0.15}As$ window layer; 200 nm p^+-GaAs; a ∼250 nm nominally undoped layer potentially containing quantum-well and/or quantum-dot structures; and 200 nm n^+-GaAs. The ∼250 nm intrinsic region consists of GaAs for reference devices; eight periods of the sequence 22 nm GaAs/8 nm $In_{0.12}Ga_{0.88}As$ in quantum-well devices; and eight periods of the sequence 22 nm GaAs/8 nm $In_{0.12}Ga_{0.88}As$/0.69 nm InAs in quantum-dot-in-well devices, where the InAs has formed quantum-dots.

Inserting quantum-wells and quantum-dots in a single-junction device brings additional considerations for its design. As heterostructures generally involve one or more strained materials, misfit dislocations can occur in layers that exceed their critical thickness and these can severely degrade photovoltaic performance by promoting carrier recombination. Strain also changes the relative positions of energy bands, effectively changing the bandgap of a material. Charge carriers must be efficiently collected throughout the device, including from quantum-well and -dot sub-band states, requiring a sufficiently strong field across the heterostructure layers [63]. This, in turn, demands that the total intrinsic layer thickness, and the doping of the p and n layers, be chosen to achieve the necessary field strength, and that the emitter and base thicknesses be chosen to achieve efficient carrier collection.

Optimal solar cells require efficient light absorption and charge carrier collection, and the use of light trapping is promising for achieving both simultaneously. Distributed Bragg reflectors have been incorporated on the bottom of quantum-well solar cells in order to achieve very high reflectivity and, as a result, improved quantum efficiency at wavelengths longer than the barrier band edge, where most light is not absorbed on its first pass across the quantum-wells [64]. Neglecting randomization of the direction of propagation of light by radiative recombination, reflective structures roughly double the path length of photons in a device, while light-scattering and -trapping structures can achieve substantially greater path length enhancements and correspondingly greater absorption.

4. Thin-film quantum-well device simulations

As modern fabrication techniques enable construction of intricate light-trapping structures, their design must eventually be guided by numerical modeling. With regard to sub-wavelength photonic and plasmonic structures, accurate modeling requires complete vectorial solutions to Maxwell's equations, which may be obtained via methods for solving

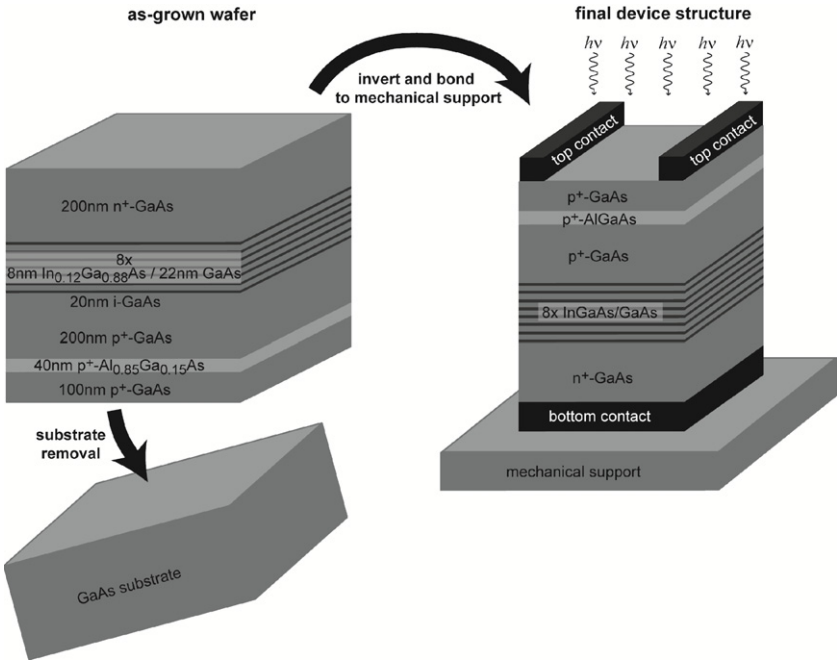

Figure 1. Schematic of the thin-film quantum-well solar cell considered in this work. The devices are fabricated by metal-bonding the epitaxial device to a mechanical support, followed by a chemical etch to remove the growth substrate, which are discussed in section 5. Similar structures have been used for a reference device, which has only GaAs in the intrinsic layer, and for a quantum-dot-in-well solar cell, which has InAs quantum-dots inserted in the $In_{0.12}Ga_{0.88}As$ quantum-wells.

partial differential equations, including finite-difference time domain (FDTD) [65], the finite element method (FEM) [66], and the Fourier modal method (also referred to as rigorous coupled-wave analysis, or RCWA) [67], which have each been applied to light trapping for photovoltaic devices.

For our work reported here, we selected an implementation of RCWA to simulate light trapping in photovoltaic devices. As this algorithm does not use a dense spatial mesh to represent the structure, solutions can be obtained efficiently for periodic structures, including gratings and photonic crystals. Perhaps the greatest utility of such simulations is in optimizing photonic structures based on design goals and observing the physical phenomena that occur in their interactions with light. The optimization process used here consisted of maximizing the short-circuit current densities of devices under the airmass (AM) 0 solar spectrum at normal incidence and for 45° linearly polarized light to account for the unpolarized nature of sunlight. Figure 2 illustrates parameters of the rear grating that have been optimized, which are the pitch (parameters L_1, L_2, W_1, and W_2), the period in the x and y directions (D_1 and D_2, respectively), and the height (H_2). Additional discussion of this procedure can be found in [68]. While the AM 0 spectrum was chosen in this instance, the optimization procedure is general and can be applied with any incident spectrum. Finally, though the performance of the rectangular grating of figure 2 was the best of several geometries that were simulated, there are likely to be designs that offer better performance, in particular for different spectral conditions.

It is important to accurately model quantum-wells and quantum-dots in these simulations as their optical properties can vary substantially from those of the corresponding

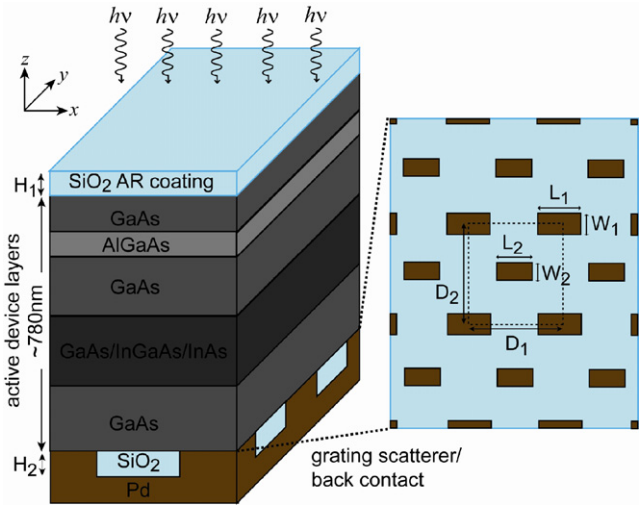

Figure 2. Diagram of the simulated device, which is equivalent in semiconductor layer structure to the experimental quantum-well solar cell shown in figure 1, and, additionally, has a broadband, two-dimensional grating located on its rear with dimensions $W_1 = 184$ nm, $L_1 = 474$ nm, $W_2 = 168$ nm, $L_2 = 356$ nm, $D_1 = 900$ nm, $D_2 = 1.13$ μm.

bulk material. Thus, calculations have been performed to incorporate the effects of quantum confinement and strain in quantum-wells and -dots. We consider the thin-film quantum-well solar cell illustrated in figure 1, which contains 8 nm thick $In_{0.12}Ga_{0.88}As$ quantum-wells that we assume are coherently strained to GaAs. In unstrained material, degeneracy of heavy- and light-hole states at the band edges results in isotropic

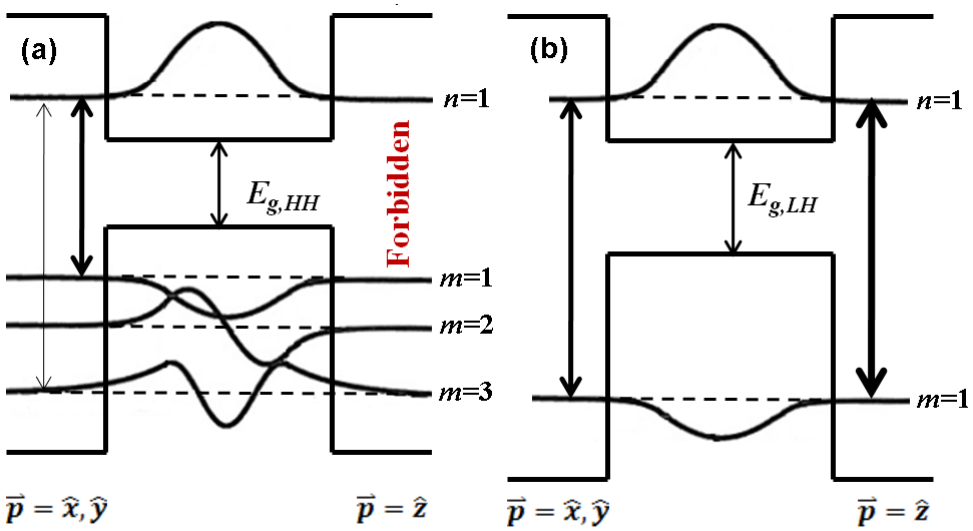

Figure 3. Radiative transitions in an 8 nm $In_{0.12}Ga_{0.88}As$ quantum-well involving (a) heavy-hole states and (b) light-hole states. The energy band gap for heavy-holes is smaller than for light-holes as a result of strain in the quantum-well. Relative transition strengths for x-, y-, and z-polarized light are indicated by the weight of arrows. A transition does not occur between $m = 2$ heavy-hole sub-band states and $n = 1$ conduction sub-band states because their envelope functions are anti-symmetric. Note that no heavy-hole transitions are allowed in quantum-wells for z-polarized light.

permittivity. Strain can lift that degeneracy, resulting in a polarization dependence of radiative transitions between the different valence bands and the conduction band and, consequently, anisotropic permittivity for a heterostructure. The magnitudes of strain-induced shifts in the band edge energies and in the band gap of bulk InGaAs can be calculated using Van de Walle's approach of deformation potentials in the framework of the model solid theory [69]. Values of the material parameters for InGaAs have been calculated by linear interpolation between the values for InAs and GaAs that are presented in that work, including the lattice and elastic constants, shear modulus, and deformation potentials.

The effects of quantum confinement are incorporated using the envelope function approximation. We assume that a quantum-well consists of a finite amount of well material surrounded by barrier material with semi-infinite spatial extent, and that there is an abrupt interface between them defined by the offsets at the valence and conduction band edges. Bulk material properties are assumed to apply up to each interface. The conduction and valence bands are treated using a four-band Kane model [70] with parabolic bands and no mixing of heavy- and light-hole states. The finite barrier heights are accounted for in calculations of bound-state energies, though it has been assumed that the envelope functions are sinusoidal over the entire width of a quantum-well and do not extend into the barriers in the calculation of the optical matrix element. Calculations of the quantum confined Stark shift in sub-band-state energies assumed an electric field in the intrinsic region of the device of 35 kV cm^{-1} at an operating voltage of 0.8 V, based on doping in the p and n regions. The resulting shifts in energy were on the order of 0.1 meV, which are negligible. The effects of strain and confinement on optical transitions in an 8 nm $In_{0.12}Ga_{0.88}As$ quantum-well, which lead to modified absorption and permittivity relative to bulk material, are illustrated in figure 3.

A semi-empirical approach has been taken with these calculations. Adapting the calculation of Nelson [71], the semi-empirical absorption coefficient for a quantum-well is found to be given by

$$\alpha(\hbar\omega) = \zeta\alpha_b \sum_{m,n} \gamma_h |\langle F_{e,n}|F_{h,m}\rangle|^2 [\theta(\hbar\omega - E_g - E_n - E_m) + r_n\delta(\hbar\omega - E_g - E_n - E_m + E_b)] \quad (1)$$

where α_b is the bulk absorption coefficient at the band edge of the quantum-well, γ_h is the relative strength of the transition as illustrated in figure 3, θ is the Heaviside function that describes the density of states, r_n is the exciton oscillator strength relative to the continuum, δ is the Dirac delta function, and ζ is a scaling factor that can be used to fit the semi-empirical calculation to measured data, though this has not been done here (i.e. $\zeta = 1$). Homogeneous broadening of excitonic transitions is modeled with a Lorentzian having a full-width at half-maximum of 2Γ. Related optical parameters, such as the semi-empirical permittivity function, may be calculated by replacing the bulk absorption coefficient at the band edge, α_b, by the equivalent value of the parameter of interest; e.g. ε_b would be used to calculate the permittivity function, which has been performed for an 8 nm $In_{0.12}Ga_{0.88}As$ quantum-well. The resulting semi-empirical values of ε_2 are shown in figure 4 and are calculated by substituting ε_b for α_b in equation (1), where ε_b has been calculated by linear interpolation between the permittivities of bulk InAs [72] and GaAs [73]. The interpolated bulk permittivity does not include effects of strain or quantum confinement; these enter through the semi-empirical calculations, which assume excitonic broadening of $\Gamma = 3$ meV, approximately the value observed for a multi-quantum-well sample [74]. The peaks in ε_2 at 965 nm and just below 950 nm in figure 4 correspond to excitonic absorption at the first heavy-hole transition and at the only light-hole transition supported by the quantum-well, respectively. At

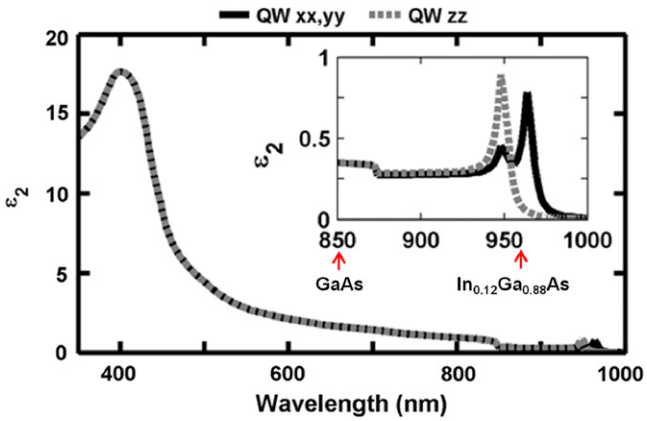

Figure 4. The component ε_2 of an 8 nm $In_{0.12}Ga_{0.88}As$ quantum-well calculated using the semi-empirical method of this paper, which results in anisotropic permittivity with (black, solid line) $\varepsilon_{2,xx} = \varepsilon_{2,yy} \neq$ (gray, dashed line) $\varepsilon_{2,zz}$. Inset: the value of ε_2 at wavelengths longer than the GaAs band edge, where peaks occur due to excitonic absorption near quantum-well sub-band edges. Arrows indicate the band edges of bulk GaAs and $In_{0.12}Ga_{0.88}As$ at 850 nm and 960 nm, respectively.

energies above the bandgap of the barrier material (in this case, GaAs), the quantum-well is assumed to have bulk material properties. This is a poor assumption at energies near the barrier band edge, but improves at higher energies as quantum effects diminish. Finally, this approach may also be used to compute the optical properties of quantum-dots by assuming that they are three-dimensional, finite quantum boxes, and works particularly well if they are strongly confined (i.e. a very thin quantum-well) in the growth direction and have less confinement in the transverse directions.

The anisotropic permittivity of 8 nm $In_{0.12}Ga_{0.88}As$ quantum-wells computed in this manner has been used in electromagnetic simulations equivalent to those in [68], which used interpolated bulk material properties for quantum-wells and -dots. Cross-sectional views of the simulated device structure are shown in figure 2. Assuming AM 0 illumination at normal incidence and collection of all photogenerated carriers, the short-circuit current density of a thin-film device made of GaAs only (i.e. containing no quantum-wells) with a planar metal backside is 28.4 mA cm^{-2}; the quantum-well solar cell with a planar metal backside generates 28.6 mA cm^{-2}; and the quantum-well solar cell with the grating shown in figure 2 generates 30.2 mA cm^{-2}. The results demonstrate that the slight benefit of adding a relatively small number of quantum-wells to a GaAs device without any light-scattering structure increases substantially with the addition of a backside grating. We also note that the relatively low indium content (12%) of the quantum-wells can be increased to enable absorption of additional infrared wavelengths, further improving photocurrent generation, and has been demonstrated for long-wavelength photodiodes [75].

The calculated absorption in the semiconductor layers of the quantum-well solar cell is shown in figure 5 as a ratio relative to absorption in a device with a planar metal backside for both the interpolated bulk material and semi-empirical quantum-well permittivities. The absorption ratios are at wavelengths shorter than 850 nm, which is expected as the semi-empirical model assumes that bulk properties apply to the quantum-well at wavelengths shorter than the GaAs band edge. At wavelengths shorter than 500 nm, GaAs and InGaAs are very strongly absorbing and all incident light is absorbed before reaching the back surface of the device. At wavelengths between 500 and 850 nm, the absorption varies due to Fabry–Pérot interference effects in the thin device structure. As these wavelengths are smaller than the period of the grating, it is essentially transparent to them and diffraction is negligible. However, the grating adds ∼140 nm of dielectric material to the device structure, which shifts the Fabry–Pérot resonances in the grating device with respect to the planar device and produces the oscillations in the absorption ratio. The effect of these shifts on the integrated photocurrent (i.e. on the short-circuit current) of a device must be considered in grating design and optimization.

Turning to longer wavelengths, as shown in figure 5(b), the effects of diffraction by the grating become evident. Most prominent are the peaks at 940, 965, and 980 nm, indicating increased absorptivity in the quantum-wells of up to a factor of 70. The spatial distribution of electric field components has been calculated and illustrates the effect of waveguiding for absorption enhancement. As radiation is incident normal to the device surface, it is polarized with the electric field in the x–y plane; a non-zero value of E_z therefore indicates a diffracted or scattered wave. In figure 6(a), which shows the steady-state value of E_z in the y–z plane of the device at an

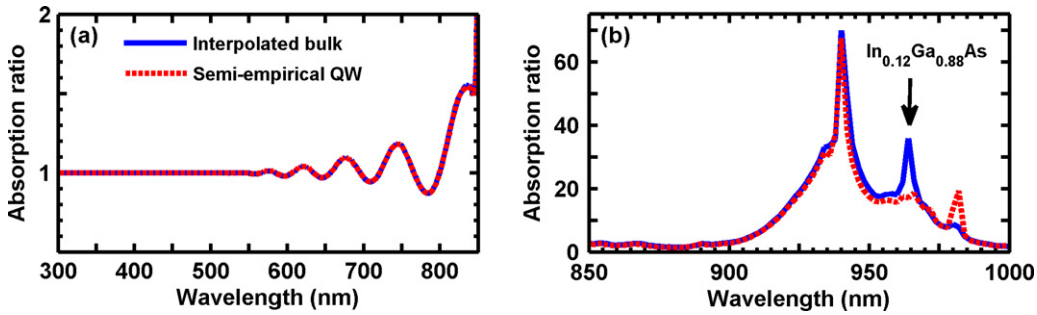

Figure 5. Spectral dependence of the ratio of absorption of incident radiation by a quantum-well solar cell with the grating of figure 2 relative to the same device with a planar backside of Pd at wavelengths (a) shorter and (b) longer than the GaAs band edge, respectively. The ratio is shown for calculations using (blue, solid line) interpolated bulk and (red, dashed line) semi-empirical quantum-well permittivity data, and the absorption edge of semi-empirical $In_{0.12}Ga_{0.88}As$ is marked.

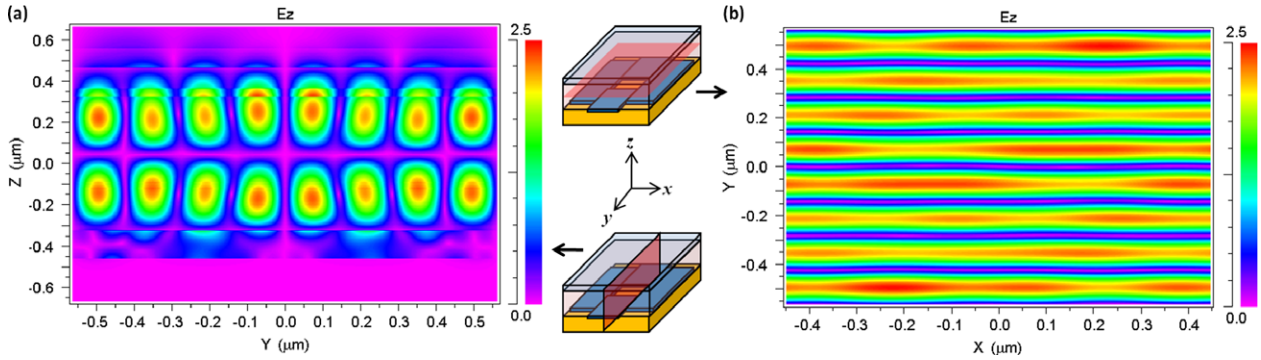

Figure 6. Calculated steady-state spatial distributions of the E_z field component for an incident wavelength of 940 nm in a thin-film quantum-well solar cell with the grating of figure 2, using the semi-empirical quantum-well permittivity data shown in figure 4, (a) the y–z plane of the device and (b) the x–y plane of the device. The fields illustrate that incident radiation at this wavelength strongly couples to a confined mode of the device structure via the grating.

incident wavelength of 940 nm, a distinct modal pattern is seen corresponding to a wave confined to the device structure. A representative cross-section of the same field component in the x–y plane is shown in figure 6(b), confirming the presence of a confined wave propagating in the y direction. Comparison of the E_x, E_y, and E_z components reveals that the strength of the confined wave can be comparable to those of unconfined waves, indicating strong coupling to the waveguide mode. The strength of coupling of incident radiation to waveguide modes of the device varies with wavelength, but coupling to the modes occurs over a broad band of wavelengths greater than the GaAs band edge (850 nm), and the effect of this is evident in the improved absorption shown in figure 5.

The absorption ratio also illustrates the importance of accurately modeling absorption in quantum confined structures. Regarding the peaks in the absorption ratio (figure 5) at wavelengths longer than 850 nm, the largest, at 940 nm, occurs both in spectra based on interpolated bulk and semi-empirical quantum-well permittivity, while those at 965 nm and at 980 nm occur only for the cases of interpolated bulk and semi-empirical quantum-well permittivity, respectively. The semi-empirical quantum-well permittivity used in these simulations, shown in figure 4 reflects the fact that the absorption in actual quantum-wells depends on the polarization of the interacting electromagnetic field. At 940 nm, where excitonic absorption is weak, the components of ε_2 for the semi-empirical quantum-well calculation are similar in value and only slightly larger than those of the interpolated bulk material. Thus, bulk material and quantum-wells exhibit similarly large increases in absorption at this wavelength.

The lack of a peak in the absorption ratio at 965 nm when semi-empirical quantum-well permittivity is used results from the polarization dependence of optical transitions in the quantum-well. While large absorption enhancement can result from coupling of incident radiation to waveguide modes with substantial E_z fields, at 965 nm $\varepsilon_{2,zz}$ for the semi-empirical permittivity is essentially zero because of a selection rule that forbids optical transitions involving heavy-hole states and z-polarized fields. The confined wave with a large E_z component is therefore weakly absorbed, leading to a modest increase in absorption in a quantum-well compared to bulk material, which absorbs light of all polarizations equally. Note that, as the bulk material permittivity does not account for excitonic effects, it is coincidental that the peak in the absorption ratio for interpolated bulk permittivity occurs at the same wavelength as the heavy-hole exciton transition, seen at 965 nm in figure 4. The absorption peak at 965 nm for interpolated bulk permittivity in figure 5 arises purely from effects of the rear grating that increase absorption in the thin-film. It may be of additional benefit if field enhancement or light scattering occurs at wavelengths corresponding to excitonic absorption in quantum-wells or -dots, where these structures are typically most strongly absorbing.

At an incident wavelength of 980 nm, the semi-empirical quantum-well absorption ratio exhibits a considerably larger peak than the interpolated bulk ratio in figure 5. Here, all components of ε_2 for the quantum-well approach zero as this wavelength is greater than its absorption edge, though it has non-zero absorptivity here as a result of homogeneous broadening of excitons. While bulk $In_{0.12}Ga_{0.88}As$ is also weakly absorbing at 980 nm, its value of ε_2 is at least an order of magnitude larger than that of the semi-empirical quantum-well calculation. As Yablonovitch demonstrated for textured surfaces [32], large absorption enhancement factors can be achieved with weakly absorbing materials, which we observe here as well. A quantum-well solar cell would benefit from a grating that facilitates strong coupling to waveguide modes at additional wavelengths shorter than the absorption edge of the quantum-wells and, in particular, that correspond to peaks in excitonic absorption. Simulations to design and optimize such gratings are being investigated.

Clearly, it is important to bear in mind the net effect of absorption enhancement, which depends on the incident spectrum, the absolute value of a material's absorptivity, and carrier collection efficiency. Achieving large absorption enhancement does not necessarily lead to a significant improvement in photocurrent generation, particularly in the weakly absorbing limit. For example, an increase in absorptivity from 0.01% to 0.5% equates to 50 times enhancement, but the absolute level of absorption remains low in both cases. As the simulations presented here illustrate,

useful improvements in the short-circuit current of thin-film, single-junction devices can be achieved by incorporating quantum-wells made of materials, such as InGaAs, that are strongly absorbing at infrared wavelengths where optimal single-junction materials, such as GaAs, are weakly absorbing, and through light trapping in such devices. Rigorous optimization of device and photonic structures in this context is a promising route to achieving significant improvements in power conversion efficiency.

5. Demonstration of thin-film solar cells

Using a substrate removal process, we have fabricated and tested thin-film GaAs solar cells, including devices that contain quantum-wells and quantum-dots-in-wells, with the device structure illustrated in figure 1. First, layers of Pd (25 nm)/Ge (10 nm)/Pd (25 nm)/In (1200 nm) are deposited on the epitaxial surface of the device wafers via electron beam evaporation, where Pd/Ge can form an ohmic contact to n-type GaAs [76]. The device wafer is placed atop a silicon wafer coated with Ti (20 nm)/Au (800 nm) such that the cleavage planes of the wafers are aligned, with the In and Au in contact, and pressure is applied manually to the wafer stack while it is heated to 25 °C on a hot plate. Bonding occurs above 160 °C, when In melts and alloys with Au [77]. Following bonding, Apiezon Wax W is applied to the sides of the wafer stack to protect them during the substrate removal etch, which consists of 19:1 H_2O_2:NH_4OH and etches GaAs preferentially to AlGaAs [78]. Following substrate removal, mesas of 1 or 4 mm^2 are patterned via photolithography and isolated using the aforementioned etch. Top contacts to the mesas are formed via photolithography, electron beam evaporation of 100 nm of Pd for an ohmic contact to p-type GaAs, and a standard lift-off.

In the case that a light-scattering structure is included on the rear of thin-film devices, it must be fabricated before bonding the device wafer to its final support. To accomplish this, first, 140 nm SiO_2 is deposited on the as-grown epitaxial device surface, followed by patterning of electron beam resist on the oxide, which is used as a mask during a CF_4/H_2 reactive ion etch of oxide to expose portions of the grating where metal is to be deposited. A thin adhesion layer of Ti is deposited immediately before the n-type GaAs contact metals previously mentioned, and under the same vacuum. The rest of the grating-equipped device fabrication is identical to the procedure above.

The spectral response of thin-film devices with and without gratings has been measured at zero bias. Measurements were performed with a single-grating monochromator based system from Optronic Laboratories using AC lock-in detection. The spectral response of devices with planar metal rear surfaces and of a quantum-dot-in-well device with a backside diffraction grating are shown in figure 7, which indicates similar performance for quantum-well and -dot-in-well solar cells at wavelengths shorter than the GaAs band edge (∼850 nm), with obvious photocurrent generation up to ∼950 nm for the quantum-well device and up to ∼1000 nm for the quantum-dot-in-well device. The level of response of quantum-well and -dot-in-well devices with planar metal

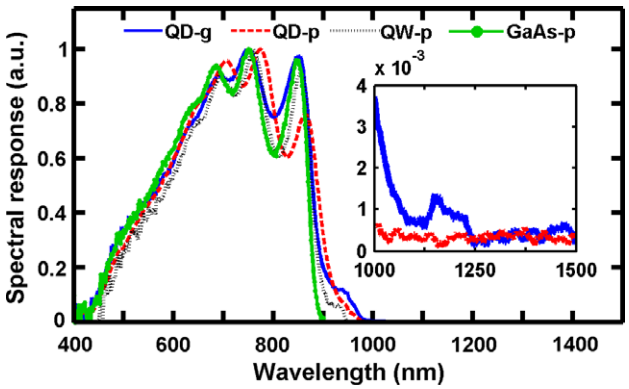

Figure 7. Normalized spectral response of thin-film devices: ('GaAs-p') pin GaAs with planar metal backside; ('QW-p') quantum-well solar cell with planar metal backside; ('QD-p') quantum-dot-in-well solar cell with planar metal backside; and ('QD-g') quantum-dot-in-well solar cell with a backside diffraction grating. Inset: the response of the grating-equipped and planar metal backside quantum-dot-in-well devices at wavelengths longer than the quantum-well absorption edge.

surfaces is quite low at wavelengths from 900 to 1000 nm due to the lack of light trapping, and increases considerably with the addition of a grating to a dot-in-well device. Also, particularly in the dot-in-well devices, carrier escape from sub-band states at zero bias is likely to be inefficient as the electric field in the dots has been calculated at 27 kV cm^{-1} using a one-dimensional Poisson solver [79]. This field is only modestly larger than the 22 kV cm^{-1} necessary for efficient carrier escape from quantum-wells with barrier heights similar to those of $In_{0.12}Ga_{0.88}As$–GaAs [63] and it is likely inadequate for the much larger InAs–GaAs barriers with quantum-dots.

The effect of the backside grating on the spectral response of thin-film devices is illustrated in figure 8, which shows the ratio of the measured response of a grating-equipped quantum-dot-in-well solar cell to that of a device with planar metal on its back surface. Also shown in figure 8 is the corresponding ratio of simulated absorption. The measurement and simulation agree closely at wavelengths shorter than 850 nm, where the only effect of the grating is to modify the thickness of the thin-film cavity, as discussed in section 4, resulting in the oscillations observed in the ratios. At wavelengths longer than 850 nm, spectral response with the grating increases as a result of enhanced absorption in quantum-wells and -dots, which results from photon path lengths increasing subsequent to diffraction by the grating. Differences in the positions of maxima in the measured and simulated response ratios likely arise from differences between the nominal thin-film device thickness and grating feature sizes and their fabricated values. Further, the waveguide consists of the semiconductor structure bounded by air on the top and metal on the bottom of the device. Imperfections at these boundaries, including roughness of the top surface following substrate removal, may degrade the quality of the waveguide, resulting in lower enhancement of the spectral response in measured devices compared to simulations. Despite these discrepancies, the simulations demonstrate that large absorption enhancements can be achieved over a broad range of wavelengths longer than

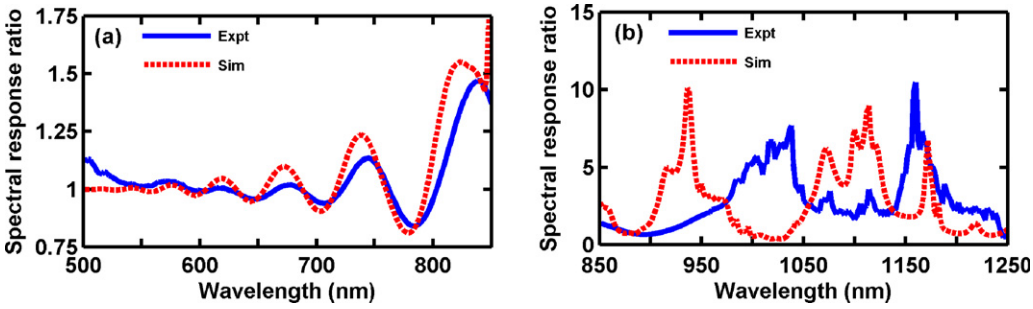

Figure 8. Ratios of ('Expt') measured spectral response and ('Sim') simulated absorption in a thin-film quantum-dot-in-well solar cell to devices with planar metal backsides at wavelengths (a) shorter and (b) longer than the GaAs band edge, respectively.

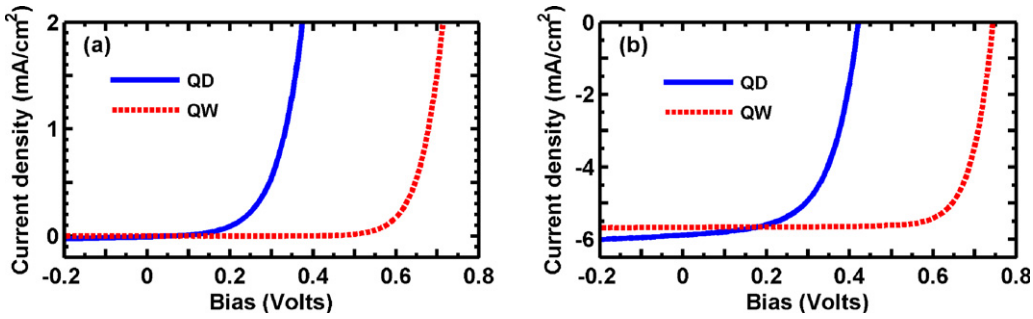

Figure 9. Current density–voltage measurements (a) in the dark and (b) under unfiltered illumination from a xenon lamp corresponding to an intensity of ∼100 mW cm^{-2}. Data are shown for a thin-film ('QW') quantum-well solar cell and for a ('QD') quantum-dot-in-well solar cell.

the GaAs absorption edge with an appropriately designed light-scattering scheme, which we confirm through experiment.

Illuminated current-density–voltage (J–V) measurements of thin-film devices with planar metal backsides have also been performed. The results, shown in figure 9, are based on illumination by a xenon lamp at an intensity of ∼100 mW cm^{-2} and without a spectral filter. As can be seen, the short-circuit current (J_{sc}) improves from 5.66 mA cm^{-2} for the quantum-well solar cell, to 5.83 mA cm^{-2} for the quantum-dot-in-well solar cell; both are improvements compared to GaAs devices, for which J_{sc} was measured to be 5.05 mA cm^{-2}. As these measurements are of devices with planar metal backsides and no light-scattering or -trapping occurs, the J_{sc} increases result from additional photocurrent generation at wavelengths longer than the GaAs band edge in quantum-wells and -dots. The reduced open-circuit voltages of quantum-dot-in-well solar cells relative to quantum-well solar cells cannot be ignored, and quantum-well devices generally exhibit voltage losses relative to control devices consisting of only barrier material in the undoped region [80]; however, strain balancing has been demonstrated to mitigate such losses in quantum-well [81] and -dot solar cells [82]. It has also been observed with quantum-well solar cells that voltage losses increase as more quantum-wells are included in the undoped region [83], so the use of light trapping with devices containing few nanostructured layers is promising to maximize performance.

The devices in this work are intended to illuminate key design considerations for quantum-well and -dot solar cells incorporating light trapping and have not been optimized for overall performance. One of the primary reasons why the measured performance of thin-film devices deviates from their simulated performance is that measured devices do not have an anti-reflection coating (ARC). The device structure of figure 2 has an approximately 100 nm thick SiO_2 ARC, which minimizes reflectivity at 580 nm, where the AM 0 photon flux is greatest. Simulations indicate that devices without an ARC have reflectivities of ∼42% at 580 nm while devices with 100 nm SiO_2 ARCs exhibit reflectivities of ∼14% at 580 nm. Also, as can be seen in figure 7, the spectral response of fabricated devices increases gradually over wavelengths 400–700 nm, which are absorbed strongly in the top 100 nm of GaAs. Simulations suggest that transport of electrons across the $Al_{0.85}Ga_{0.15}As$ window is poor, which may be a result of the large potential barrier for electrons at the GaAs–AlGaAs interface. As solar irradiance peaks below 700 nm, the combined effects of having no ARC and poor carrier transport across the window significantly diminish the short-circuit currents of measured devices from their optimal values, which simulations indicate should approach 30 mA cm^{-2}.

6. Summary

In summary, solar cells benefit greatly from approaches that combine efficient light absorption and charge carrier collection, which can be addressed simultaneously with thin-film devices that use semiconductor nanostructures and photonic structures for light trapping. Rigorous electromagnetic and electrical simulations that account for material properties and the complete spectral conditions to

which solar cells are exposed are required to optimize their performance over the total range of their spectral response. We have used electromagnetic simulations with a realistic model of absorption in quantum-wells to demonstrate the importance of such an approach and that the use of quantum-wells or quantum-dots, combined with optimal light-trapping schemes, is a promising route to creating efficient, thin-film devices. Fabricated thin-film solar cells demonstrate that the insertion of $In_{0.12}Ga_{0.88}As$ quantum-wells, or of the same quantum-wells with embedded InAs quantum-dots, in the active region of a GaAs device extends its spectral response by ∼50 nm and ∼150 nm, respectively, with corresponding increases in short-circuit current. Simulations indicate that the thin-film quantum-well solar cell with a backside diffraction grating displaying broadband functionality exhibits a 6% increase in short-circuit current under the AM 0 spectrum. Measurements of thin-film quantum-dot-in-well solar cells with such a grating demonstrate broadband enhancement of spectral response to wavelengths above 1200 nm and corroborate simulated absorption enhancement. Additional improvements should be achievable via optimization that uses realistic optical parameters for quantum-wells and quantum-dots.

Acknowledgments

COM gratefully acknowledges support from a NASA GSRP fellowship, helpful discussions with K Vijayraghavan and R Adams, and assistance with measurements from K W Park. Part of this work was supported by the National Science Foundation (DMR 0806755 and DMR 1066430), the Department of Energy (DE-FG36-08G018016), and the Judson S Swearingen Regents Chair in Engineering at the University of Texas at Austin.

References

[1] Heine C and Morf R H 1995 *Appl. Opt.* **34** 2476
[2] Lee Y C, Huang C F, Chang J Y and Wu M L 2008 *Opt. Express* **16** 7969
[3] Naqavi A, Söderström K, Haug F J, Paeder V, Scharf T, Herzig H P and Ballif C 2011 *Opt. Express* **19** 128
[4] Schaadt D M, Feng B and Yu E T 2005 *Appl. Phys. Lett.* **86** 063106
[5] Catchpole K R and Pillai S 2006 *J. Appl. Phys.* **100** 044504
[6] Derkacs D, Lim S H, Matheu P, Mar W and Yu E T 2006 *Appl. Phys. Lett.* **89** 093103
[7] Nakayama K, Tanabe K and Atwater H A 2008 *Appl. Phys. Lett.* **93** 121904
[8] Mokkapati S, Beck F J, Polman A and Catchpole K R 2009 *Appl. Phys. Lett.* **95** 053115
[9] O'Brien P G, Kherani N P, Zukotynski S, Ozin G A, Vekris E, Tetreault N, Chutinan A, John S, Mihi A and Míguez H 2007 *Adv. Mater.* **19** 4177
[10] Bermel P, Luo C, Zeng L, Kimerling L C and Joannopoulos J D 2007 *Opt. Express* **15** 16986
[11] Duché D, Escoubas L, Simon J, Torchio P, Vervisch W and Flory F 2008 *Appl. Phys. Lett.* **92** 193310
[12] Suezaki T, Yano H, Hatayama T, Ozin G A and Fuyuki T 2011 *Appl. Phys. Lett.* **98** 072106
[13] Barnham K W J, Braun B, Nelson J, Paxman M, Button C, Roberts J S and Foxon C T 1991 *Appl. Phys. Lett.* **59** 135
[14] Jani O, Ferguson I, Honsberg C and Kurtz S 2007 *Appl. Phys. Lett.* **91** 132117
[15] Farrell R M, Neufeld C J, Cruz S C, Lang J R, Iza M, Keller S, Nakamura S, DenBaars S P, Mishra U K and Speck J S 2011 *Appl. Phys. Lett.* **98** 201107
[16] Laghumavarapu R B, El-Emawy M, Nuntawong N, Moscho A, Lester L F and Huffaker D L 2007 *Appl. Phys. Lett.* **91** 243115
[17] Hubbard S M, Cress C D, Bailey C G, Raffaelle R P, Bailey S G and Wilt D M 2008 *Appl. Phys. Lett.* **92** 123512
[18] Popescu V, Bester G, Hanna M C, Norman A G and Zunger A 2008 *Phys. Rev.* B **78** 205321
[19] Huynh W U, Dittmer J J and Alivisatos A P 2002 *Science* **295** 2425
[20] Law M, Greene L E, Johnson J C, Saykally R and Yang P 2005 *Nature Mater.* **4** 455
[21] Tsakalakos L, Balch J, Fronheiser J, Korevaar B A, Sulima O and Rand J 2007 *Appl. Phys. Lett.* **91** 233117
[22] Kupec J, Stoop R L and Witzigmann B 2010 *Opt. Express* **18** 27589
[23] Wei G, Shiu K T, Giebink N C and Forrest S R 2007 *Appl. Phys. Lett.* **91** 223507
[24] Bremner S P, Corkish R and Honsberg C B 1999 *IEEE Trans. Electron Devices* **46** 1932
[25] Luque A and Marti A 1997 *Phys. Rev. Lett.* **78** 5014
[26] Schaller R D and Klimov V I 2004 *Phys. Rev. Lett.* **92** 186601
[27] Shockley W and Queisser H J 1961 *J. Appl. Phys.* **32** 510
[28] Otte K, Makhova L, Braun A and Konovalov I 2006 *Thin Solid Films* **511/512** 613
[29] Krebs F C, Jørgensen M, Norrman K, Hagemann O, Alstrup J, Nielsen T D, Fyenbo J, Larsen K and Kristensen J 2009 *Sol. Energy Mater. Sol. Cells* **93** 422
[30] Schermer J J, Mulder P, Bauhuis G J, Voncken M M A J, van Deelen J, Haverkamp E and Larsen P K 2005 *Phys. Status Solidi* a **202** 501
[31] Lee K, Shiu K T, Zimmerman J D, Renshaw C K and Forrest S R 2010 *Appl. Phys. Lett.* **97** 101107
[32] Yablonovitch E 1982 *J. Opt. Soc. Am.* **72** 899
[33] Campbell P and Green M A 1987 *J. Appl. Phys.* **62** 243
[34] Gee J M 2002 *Proc. 29th IEEE Photovolt. Spec. Conf.* p 150
[35] Saeta P N, Ferry V E, Pacifici D, Munday J N and Atwater H A 2009 *Opt. Express* **17** 20975
[36] Yu Z, Raman A and Fan S 2010 *Proc. Natl Acad. Sci. USA* **107** 17491
[37] Chang T H, Wu P H, Chen S H, Chan C H, Lee C C, Chen C C and Su Y K 2009 *Opt. Express* **17** 6519
[38] Derkacs D, Chen W V, Matheu P M, Lim S H, Yu P K L and Yu E T 2008 *Appl. Phys. Lett.* **93** 091107
[39] Matheu P, Lim S H, Derkacs D, McPheeters C O and Yu E T 2008 *Appl. Phys. Lett.* **93** 113108
[40] Chan C H *et al* 2005 *Nanotechnology* **16** 1440–4
[41] Jiang P, Prasad T, McFarland M J and Colvin V L 2006 *Appl. Phys. Lett.* **89** 011908
[42] Jeong S, Hu L, Lee H R, Garnett E, Choi J W and Cui Y 2010 *Nano Lett.* **10** 2989
[43] Bohren C F and Huffman D R 1984 *Absorption and Scattering of Light by Small Particles* (New York: Wiley)
[44] Hu L and Chen G 2007 *Nano Lett.* **7** 3249
[45] Tsakalakos L *et al* 2007 *J. Nanophoton.* **1** 013552
[46] Tena-Zaera R, Elias J and Lévy-Clément C 2008 *Appl. Phys. Lett.* **93** 233119
[47] Lim S H, Mar W, Matheu P, Derkacs D and Yu E T 2007 *J. Appl. Phys.* **101** 104309
[48] Chou S Y, Krauss P R and Renstrom P J 1995 *Appl. Phys. Lett.* **67** 3114
[49] Hulteen J C and Van Duyne R P 1995 *J. Vac. Sci. Technol.* A **13** 1553
[50] Xia Y and Whitesides G M 1998 *Annu. Rev. Mater. Sci.* **28** 153

[51] Mutitu J G, Shi S, Chen C, Creazzo T, Barnett A, Honsberg C and Prather D W 2008 *Opt. Express* **16** 15238
[52] Ferry V E, Verschuuren M A, Li H B T, Schropp R E I, Atwater H A and Polman A 2009 *Appl. Phys. Lett.* **95** 183503
[53] Fahr S, Rockstuhl C and Lederer F 2008 *Appl. Phys. Lett.* **92** 171114
[54] Lin A and Phillips J 2008 *Sol. Energy Mater. Sol. Cells* **92** 1689
[55] Martí A, Antolín E, Stanley C R, Farmer C D, López N, Díaz P, Cánovas E, Linares P G and Luque A 2006 *Phys. Rev. Lett.* **97** 247701
[56] Luque A, Martí A and Nozik A J 2007 *MRS Bull.* **32** 236
[57] Sambur J B, Novet T and Parkinson B A 2010 *Science* **330** 63
[58] Neave J H, Dobson P J, Harris J J, Dawson P and Joyce B A 1983 *Appl. Phys.* A **3** 195
[59] Ploog K 1981 *Annu. Rev. Mater. Sci.* **11** 171
[60] Hu D Z, Trampert A and Schaadt D M 2010 *J. Cryst. Growth* **312** 447
[61] Reithmaier J P, Riechert H, Schlötterer H and Weimann G 1991 *J. Cryst. Growth* **111** 407
[62] Hu D, McPheeters C O, Yu E T and Schaadt D M 2011 *Nanoscale Res. Lett.* **6** 83
[63] Alemu A, Coaquira J A H and Freundlich A 2006 *J. Appl. Phys.* **99** 084506
[64] Bushnell D B, Ekins-Daukes N J, Barnham K W J, Connolly J P, Roberts J S, Hill G, Airey R and Mazzer M 2003 *Sol. Energy Mater. Sol. Cells* **75** 299
[65] Tavlove A 1995 *Computational Electrodynamics: The Finite-Difference Time-Domain Method* (Norwood, MA: Artech House Publishers)
[66] Jin J 2002 *The Finite Element Method In Electromagnetics* 2nd edn (New York: Wiley)
[67] Petit R 1989 *Electromagnetic Theory of Gratings* (Berlin: Springer) p 174
[68] McPheeters C O, Hill C J, Hu D, Lim S H, Derkacs D, Ting D Z, Schaadt D M, Gunapala S D and Yu E T 2010 *Proc. SPIE* **7772** 777209
[69] Van de Walle C G 1989 *Phys. Rev.* B **39** 1871
[70] Kane E O 1957 *J. Phys. Chem. Solids* **1** 249
[71] Nelson J 2001 *Low-dimensional Semiconductor Structures: Fundamentals and Device Applications* ed K Barnham and D Vvedensky (Cambridge: Cambridge University Press) p 209
[72] Adachi S 1987 *Phys. Rev.* B **35** 7454
[73] Palik E D 1998 *Handbook of Optical Constants of Solids* (San Diego, CA: Academic)
[74] Shen W Z, Shen S C, Tang W G, Wang S M and Andersson T G 1995 *J. Appl. Phys.* **78** 1178
[75] Dries J G, Gokhale M R and Forrest S R 1999 *Appl. Phys. Lett.* **74** 2581
[76] Marshall E D, Chen W X, Wu C S, Lau S S and Keuch T F 1985 *Appl. Phys. Lett.* **47** 298
[77] Lee C C, Wang C Y and Matijasevic G 1993 *IEEE Trans. Compon. Hybrids Manuf. Technol.* **16** 311
[78] Carter-Coman C, Bicknell-Tassius R, Benz R G, Brown A S and Jokerst N M 1997 *J. Electrochem. Soc.* **144** L29
[79] Snider G 2011 *1D Poisson* http://www.nd.edu/~gsnider/ accessed 7 August 2011
[80] Barnham K, Ballard I, Barnes J, Connolly J, Griffin P, Kluftinger B, Nelson J, Tsui I and Zachariou A 1997 *Appl. Surf. Sci.* **113/114** 722
[81] Ekins-Daukes N J, Barnham K W J, Connolly J P, Roberts J S, Clark J C, Hill G and Mazzer M 1999 *Appl. Phys. Lett.* **75** 4195
[82] Bailey C G, Forbes D V, Raffaelle R P and Hubbard S M 2011 *Appl. Phys. Lett.* **98** 163105
[83] Bushnell D B, Tibbits T N D, Barnham K W J, Connolly J P, Mazzer M, Ekins-Daukes N J, Roberts J S, Hill G and Airey R 2005 *J. Appl. Phys.* **97** 124908